Microstructural and Mechanical Characterization of Thin-Walled Tube Manufactured with Selective Laser Melting for Stent Application

E. Langi, L.G. Zhao, P. Jamshidi, M.M. Attallah, V.V. Silberschmidt, H. Willcock, and F. Vogt

This paper focuses on microstructural and mechanical characterization of metallic thin-walled tube produced with additive manufacturing (AM), as a promising alternative technique for the manufacturing of tubes as a feedstock for stents micromachining. Tubes, with a wall thickness of 500 μm, were made of 316L stainless steel using selective laser melting. Its surface roughness, constituting phases, underlying microstructures and chemical composition were analyzed. The dependence of hardness and elastic modulus on the crystallographic orientation were investigated using electron backscatter diffraction and nanoindentation. Spherical nanoindentation was performed to extract the indentation stress–strain curve from the load–displacement data. The obtained results were compared with those for a commercial 316L stainless steel stent. Both tube and commercial stent samples were fully austenitic, and the as-fabricated surface finish for the tube was much rougher than the stent. Microstructural characterization revealed that the tube had a columnar and coarse grain microstructure, compared to equiaxed grains in the commercial stent. Berkovich nanoindentation suggested an effect for the grain orientation on the hardness and Young's modulus. The stress–strain curves and the indentation yield strength for the tube and stent were similar. The work is an important step toward AM of patient-specific stents.

1. Introduction

Stenosis is a gradual build-up of fatty (atheroma) and calcified (sclerotic) deposits inside the arteries in a process called atherosclerosis, the principal cause of cardiovascular disease (CVD) and myocardial infarction. Cardiovascular diseases (CVDs) are the number 1 cause of death globally, representing 31% of all global deaths, and 85% of all CVD deaths are due to heart attacks and strokes (Ref 1). Balloon angioplasty was first performed by Andreas Gruntzig in 1977, starting a revolution in the treatment of stenosis. However, the outcomes were compromised by an occurrence of vessel blockage triggered by acute arterial recoil and intima hyperplasia (restenosis) (Ref 2). The development of stents, i.e., scaffolds made of metallic alloys or biopolymers, began in the mid-1980s, aiming to prevent restenosis and arterial recoil related to balloon angioplasty. Stents proved effective in sustaining the blood vessels once expanded inside diseased arteries. Development of stents went through the stages of bare-metal stents (BMSs; (Ref 3, 4), drug-eluting stents (DESs; (Ref 5, 6) and bioresorbable stents (BRSs; (Ref 7); as of today, stent implantation has become one of the most common medical procedures worldwide with more than 1 million procedures performed annually in Europe alone (Ref 8). Studies (Ref 9, 10) showed that different types of stents triggered different vascular response and, as a result, several desirable attributes were identified for stents, including low recoil, low surface roughness (with Ra value less than 0.5 μm), biocompatibility, thinner struts and optimal cell design. Currently, thin-strut DESs, made of metallic alloys such as Co-Cr alloy and coated with drugs, remain the favorable recommendations for treating patients with severe stenosis, thanks to their superiority in preventing in-stent restenosis (re-narrowing of the blood vessel due to intima hyperplasia) and late stent thrombosis (associated with less biocompatible materials and bulky struts such as in polymeric BRSs).

The most commonly used fabrication technology for stents is laser machining (Ref 11), which employs a laser to cut the stent profile from a thin-walled tube. The stents produced by laser machining have uniform geometries in terms of stent diameter, cell design and strut size. The current stenting of diseased arteries involves the use of off-the-shelf stents, and the lack of lesion-specific stents raises the potential risk of suboptimal stent deployment in the diseased artery. This is particularly true when treating diseased arteries with severely calcified plaques, resulting in low lumen areas and undesirable shapes. Furthermore, the progression of stenosis, plaque composition, shape and mechanical properties can vary considerably, and plaque's histological types were found to have a statistical difference in their radial compressive stiffness, for which the use of the off-the-shelf stents is not ideal (Ref 12).

E. Langi, L.G. Zhao, and **V.V. Silberschmidt**, Wolfson School of Mechanical, Electrical and Manufacturing Engineering, Loughborough University, Epinal Way, Loughborough LE11 3TU, UK; **P. Jamshidi** and **M.M. Attallah**, School of Metallurgy and Materials, University of Birmingham, Edgbaston, Birmingham B15 2TT, UK; **H. Willcock**, Department of Materials, Loughborough University, Epinal Way, Loughborough LE11 3TU, UK; and **F. Vogt**, Medical Clinic I, RWTH University Hospital Aachen, Pauwelsstrasse 30, 52074 Aachen, Germany. Contact e-mail: L.Zhao@Lboro.ac.uk.

Lesion-specific properties such as shape and stiffness must be considered in stent design. So, there is a need to develop lesion-specific stents, with varied design, diameter and strut size, for much improved clinical outcomes. This can be achieved via AM (Ref 13). AM based on SLM can be used to produce stents directly from powder in a single process, eliminating the need for hollow tube manufacturing and laser micro-cutting age. As a result, the processing complexities reduce and, in turn, cut down the processing time and production costs. In SLM, a laser beam is used as an energy source to melt metallic powder bed layer by layer to produce the desired geometry according to the CAD profile, with a great potential to produce patient-specific medical devices (Ref 14).

In literature, AM of vascular devices was largely limited to polymeric materials, together with the processes such as fused deposition modeling, binder jetting and stereolithography processes. Still, shown in Centola et al. (Ref 15), it remains a challenge for the polymeric scaffolds to maintain structural and functional integrity immediately after implantation due to the weak mechanical properties of the material. Moore et al. (Ref 16) printed a lesion-specific polymeric stent with strut sizes in the range 120–200 μm; however, there were inherent weaknesses in the printed part due to the layer by layer build mechanism. On expansion, the strut failed due to linear delamination along the z-plane (vertical axis). As a consequence of increased rates of reinterventions, the principal BRS, the Absorb Bioresorbable Vascular Scaffold (BVS) was pulled from the worldwide market in 2017 (Ref 17). Thus, more recently, the use of AM for manufacturing metallic stents has started gaining attention. Wessarges et al. (Ref 18) produced a prototype SLMed 316L stainless steel (316L SS) stent with a 60 μm strut size. Balloon expansion of this stent was executable, but the SEM inspection of expanded stent showed micro-cracks close to the strut junction in some of the tested samples. Demir et al. (Ref 19) also produced prototype stents from CoCr alloy powder using the SLM process with the strut sizes in the range 340–380 μm. The x-ray computed tomography of the cross section depicted full density and the prototype stent was free of internal pores. However, the average roughness, Ra, value (10.5–13 μm) for the produced stent was higher than the surface finish conventionally required for stents (Ra < 0.5 μm). Finazzi et al. (Ref 20) produced CoCr metal stents using SLM with the strut sizes in the range 90–120 μm. There were no macro-defects detected in the manufactured stents. Electrochemical polishing was used to effectively reduce the average roughness from 8.4 μm to 2.2 μm. The achieved values indicated an important reduction in surface roughness but still, further reduction in Ra is required to fit the surface requirement for stents. The selective laser melted (SLMed) CoCr stent was able to expand twice its initial diameter, in both as-built and electropolished conditions, without any fracture. Clearly, AM of stents was proved in literature, but the full potential of producing metallic stents through SLM is yet to be discovered, especially with regard to the microstructure and its connection with mechanical properties, which are essential for commercialization of the technology.

This paper investigates the underlying microstructure and mechanical properties of a thin-walled structure manufactured from 316L SS using the SLM process for stent application, i.e., as a feedstock for stent micromachining. A full comparison with a commercial stent was conducted, which is critical for evaluating the potential of AM for stent production. Specifically, the surface roughness was assessed quantitively, followed by characterization using scanning electron microscopy (SEM)/electron backscatter diffraction (EBSD). The mechanical properties were measured based on spherical nanoindentation, which allowed for the extraction of hardness, Young's modulus and stress-strain responses, in connection with underlying microstructures. Comparatively, the results were used to address the challenges in the employing of AM technique for fabricating microscale structures.

2. Materials and Methods

2.1 Samples

Samples of 316L SS thin-walled tube and commercial 316L SS stent were used in this study; they are referred to simply as *tube* and *stent*. The stent (Multi-Link RX Ultra™ of Abbott; 100 μm strut size) was used as a reference material for comparison. The tube was produced by AM using a Concept laser M2 cusing system. They were built on a steel substrate in 99.99% pure Argon atmosphere controlled to <100 ppm of oxygen. Unlike other platforms (e.g., Renishaw systems), the system is not vacuumed prior to argon purging since it is not pressure tight. The limited amount of oxygen in the chamber due to the fluctuations in flowing argon might cause a slight discoloration in the builds. The M2 system has a Yb-fiber laser, with laser power up to 400 W, 60 μm laser spot size, a track width of 150 μm and a scan speed up to 7000 mm/s. The 316L SS steel powder supplied by Atomising Systems Ltd (Sheffield, UK) was used as a feedstock material. The powder size was in the range 15–53 μm with an average size of 32 μm. A laser power of 100 W, a layer thickness of 20 μm and a scan speed of 1600 mm/s were used to build a thin-walled structure of 8 mm in diameter, 30 mm height, 500 μm thickness in an argon protective atmosphere. Neither heat treatment nor etching was conducted on the thin tube. Figure 1 shows the tube and Multi-Link RX Ultra™ stent of Abbott used in this study.

2.2 Surface Roughness

The surface roughness of the samples was characterized using the focus variation technique by Alicona Infinite, that combines a small depth of focus of an optical system with vertical scanning to produce a topographic model of the surface. In this study, a 10× objective lens was used, with a 1.4 mm × 1.0 mm field of view, a 2 μm lateral resolution, a 17 mm stand-off distance and a 1 μm vertical resolution. The examined roughness parameters were average roughness Ra, root-mean-square Rq and the mean roughness depth Rz.
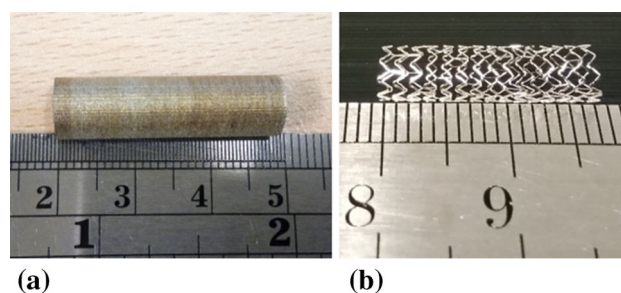

Fig. 1 (a) Tube with a ~ 500 μm wall thickness; (b) Multi-Link RX Ultra stent of Abbott with a 100 μm strut thickness

2.3 XRD Analyses

X-ray diffraction (XRD) was used to characterize the phase content of the samples, using a Bruker D8 x-ray diffractometer. The two samples were cut using a Struer slow speed cutter and a small sharp wire cutter and then flattened. The samples were cleaned with acetone and then rinsed with deionized water. The diffractometer used Cu-Kα radiation, operating at a voltage of 30 kV and a current of 10 mA. A fixed detector slit size of 0.3 mm × 12 mm was used. Before the XRD scan, the z-scan was used to correct the height on the z-drive. The sample was then locked in position, and the scan was performed at a step size of 0.02° with 2θ kept in the range of 30° and 120°. The diffraction patterns obtained were plotted with intensity against 2θ. The JCPDS-cards 31-0619 and 06-0696 were used for identification of different phases in the samples.

The dislocation density was then measured using the Williamson and Hall method (Ref [21]). In this method, the internal strain ε and crystallite size D of the samples were calculated by using XRD patterns,

$$\beta \cos \theta = \varepsilon (4 \sin \theta) + \frac{k\lambda}{D}, \qquad \text{(Eq 1)}$$

where β, θ, λ, D and ε are the physical broadening of full width at half maximum (FWHM) of the diffraction peak, the Bragg angle, the wavelength of the radiation, crystallite size and internal strain, respectively. Equation [1] has the form $y = mx + c$, in which ε is the slope and the y-intercept is $\frac{k\lambda}{D}$. Dislocation density (ρ) was then calculated by

$$\rho = A \frac{\varepsilon^2}{b^2}, \qquad \text{(Eq 2)}$$

where b is the Burgers vector (0.25 nm for SLMed 316L SS) and $A = 16.1$ is a constant.

2.4 Microstructural Characterization

Detailed microstructural characterization of the samples was performed using both an optical microscope (OM, Zeiss Primotech) and a field emission scanning electron microscope (SEM JEOL 7800). The samples were cut into pieces, approximately 4 mm in length, and then cold mounted using epoxy resin and conductive filler (Buehler) in a 1:1 ratio. Using a Buehler Automet-250 machine, the samples were mechanically ground with 1200 grit silicon carbide paper and polished with diamond pastes of 9, 3 and 1 μm. The final preparation involved vibro-polishing of the samples using MasterMet 2 Colloidal Silica to chemo-mechanically polish the samples. For optical microscopy and SEM examinations, the samples were etched by immersion in a solution of 8.5 g FeCl$_3$, 2.4 g CuCl$_2$, 122 mL hydrochloric acid, 6 mL nitric acid and 122 mL ethanol for 30 s.

EBSD was performed using SEM JEOL 7800 equipped with an Oxford Nordlys II S EBSD detector and HKL Channel 5.0 EBSD postprocessing software. The specimen was tilted to 70° and kept at a working distance of 10 mm. The microscope was operating at a 20-kV acceleration voltage and a 0.5 μm step size. The EBSD analyses were used to provide crystallographic information on individual grains and the associated grain boundary misorientation angles. The grain size for the samples was approximated by the diameter of a circle with an equal surface area.

In addition, energy-dispersive x-ray spectroscopy (EDS) affiliated with the SEM was used to detect the chemical composition of the samples. In this work, we used standardless quantification and ZAF correction methods. ZAF corrections were applied to EDX measurements in the SEM to convert apparent concentrations (raw peak intensity) into (semi-quantitative) concentrations considering inter-element matrix effects. The EDS x-ray analysis system is installed with default spectra (Oxford instruments) for all the elements and the commonly used x-ray analysis lines. The default data enabled an estimation of the composition for the spectra collected, and this information was useful in identifying the phases in the sample. It must be mentioned that quantification of light elements such as carbon and oxygen is a challenge due to the limited sensitivity of EDS and therefore omitted in this study. Elemental composition of the samples was collected for 100 s at 10 mm working distance, using an accelerating voltage of 20 kV. The EDS spectra were analyzed with the Aztec software, and the data of the chemical composition were presented normalized to 100%.

2.5 Nanoindentation Testing

Further to the microstructural and crystallographic investigations, nanoindentation was performed to extract mechanical properties using the Berkovich and spherical indenter tips. The tests were performed with the NanoTest Platform 3 machine (Micromaterial, Wrexham UK). The tip area function was calibrated by indenting fused silica, where the tip has the Young's modulus of 1140 GPa and the Poisson's ratio of 0.07. The sample preparation for nanoindentation was the same as the one outlined in "Microstructural Characterization" section above for SEM and EBSD tests.

2.5.1 Berkovich Nanoindentation. The Berkovich nanoindentation tests were conducted to determine the hardness and elastic modulus of the samples. The samples were indented perpendicular to their respective surfaces under load controlled and fixed time conditions. The load level was chosen to be 3, 7, 10, 15 and 25 mN. The loading and unloading times were 10 s, and a 10 s dwell time was imposed at the peak load. A 4 × 4 grid of indents at each load was performed with a 15 μm spacing in two orthogonal directions. Oliver and Pharr's methods (Ref [22]) were used to calculate the hardness, H, and effective Young's modulus, E_{eff}, after a complete loading–unloading cycle. To study the effect of grain orientation on hardness and the Young's modulus, EBSD was performed after nanoindentation. At each indentation point, orientation in terms of Bunge–Euler angles was extracted using the HKL Channel 5.0 EBSD postprocessing software.

2.5.2 Spherical Nanoindentation. Nanoindentation was also performed with a spherical indenter with the tip radius of 10 μm to extract stress–strain responses. For this test, 20 loading–unloading indentation cycles were conducted on the samples. The protocols used in this study to extract the indentation stress–strain curves (Ref [22–25]) are based on the Hertz theory. The Hertz's theory can be modified to give a relationship between indentation stress and strain defined as:

$$\sigma_{\text{ind}} = E_{\text{eff}} \varepsilon_{\text{ind}}, \quad \sigma_{\text{ind}} = \frac{P}{\pi a^2}, \quad \varepsilon_{\text{ind}} = \frac{4}{3\pi} \frac{h_t}{a} \approx \frac{h_t}{2.4a}, \quad \text{(Eq 3)}$$

where P, a, σ_{ind}, ε_{ind}, E_{eff} are the load, contact radius, indentation stress, indentation strain and effective modulus. The

indentation yield strength, Y_{ind}, was defined using a 0.2% offset plastic strain on the indentation stress–strain curve.

3. Results

3.1 Surface Roughness

Surface morphology can have a significant influence on the mechanical properties of the stent. As a result, the effect of AM on the surface quality of the printed tube was analyzed first. Figure 2(a) shows focus variation of the tube in as-built condition and Fig. 2(b) presents the variation for stent. Figures 2(c) and (d) report the surface profiles for the tube and stent with the scanned path length of 5.089 and 1.159 mm, respectively. The average roughness Ra, root-mean-square roughness Rq and mean roughness depth Rz for the tube were 6.68, 8.38 and 43.26 μm, respectively. In the same vein, the roughness parameters for the stent were 0.18, 0.26 and 1.23 μm, respectively. These results demonstrated a significant difference in terms of surface roughness parameters between the two samples. Surface finish conventionally required for stents is Ra $<$ 0.5 μm (Ref 20). Even though SLM gave a fine geometry precision for the tube, its surface topography is still a drawback, requiring attention such as the use electrochemical etching to improve the surface finish. The average surface roughness value Ra for the stent was well below the recommended one since the sample was exposed to the surface finishing process such as etching and electropolishing.

3.2 Composition and Phases

The composition for tube and stent and their crystallographic phases were thoroughly analyzed next. Figure 3(a) depicts a representative XRD plot for the tube and stent. The recorded XRD pattern had sharp peaks with a good match with austenite (FCC) phase. The results of XRD analyses of the tube revealed the presence of only a single austenite phase. In contrast, the XRD pattern of the stent showed traces of the second phases such as δ-ferrite, α-within the detection limit of x-ray diffraction. Other studies (Ref 26, 27) also reported the formation of single-phase austenite in SLMed 316L SS. The formation of pure austenite phase in the tube is attributed to a high cooling rate and its variations in different regions. However, Saeidi et al. (Ref 26) reported the formation of a second phase (ferrite) after conducting heat treatment at 1100°C for one hour followed by furnace cooling and attributed this to solute partitioning. The difference in the relative intensities of different peaks between tube and the stent indicated the presence of crystallographic texture in the SLMed tube with preferential growth. Using the Williamson–Hall method, internal strain (ε) for the tube and stent was calculated to be 0.186% and 0.099%, respectively (Fig. 3b, c). The dislocation density for the tube and stent were estimated to be 8.57×10^{14} and 2.44×10^{14} m^{-2}, respectively. Furthermore, the peaks for the tube were broader compared to those of the stent because of the presence of high internal strains and dislocations introduced during the SLM process.
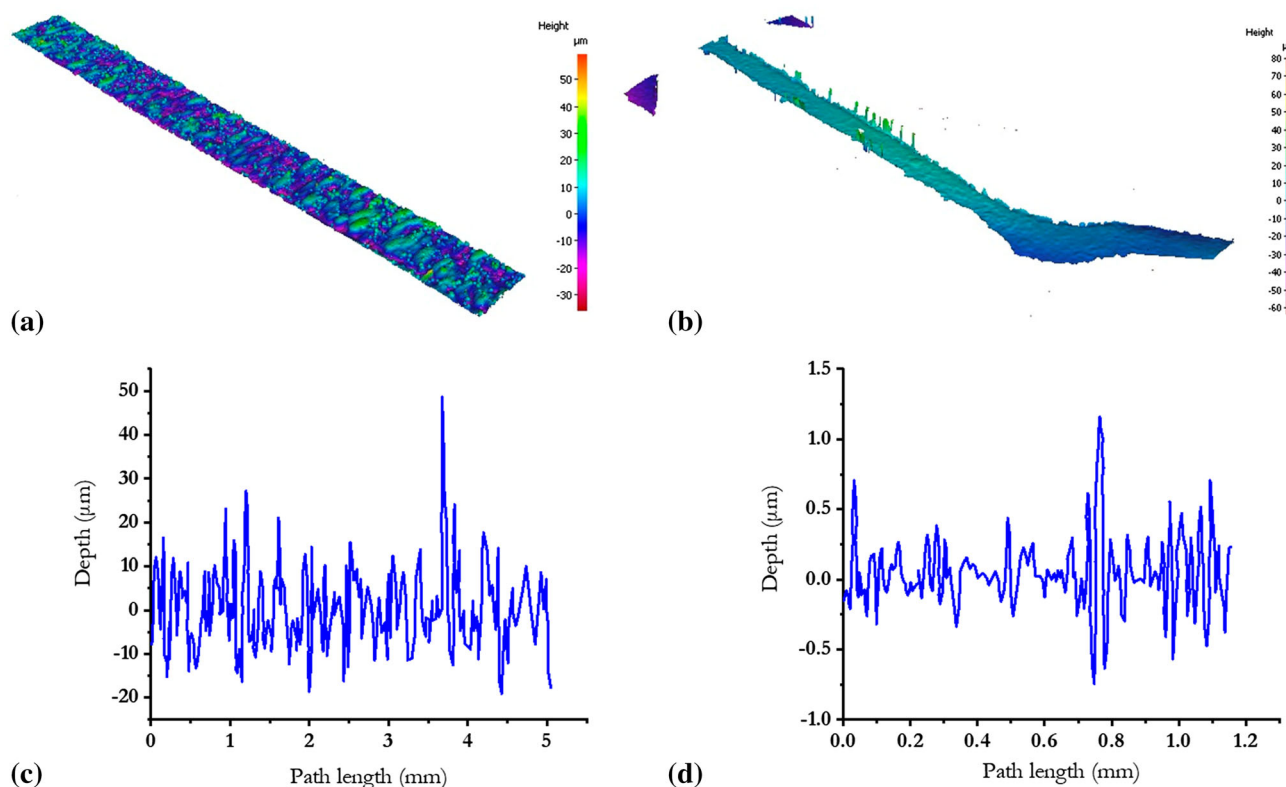

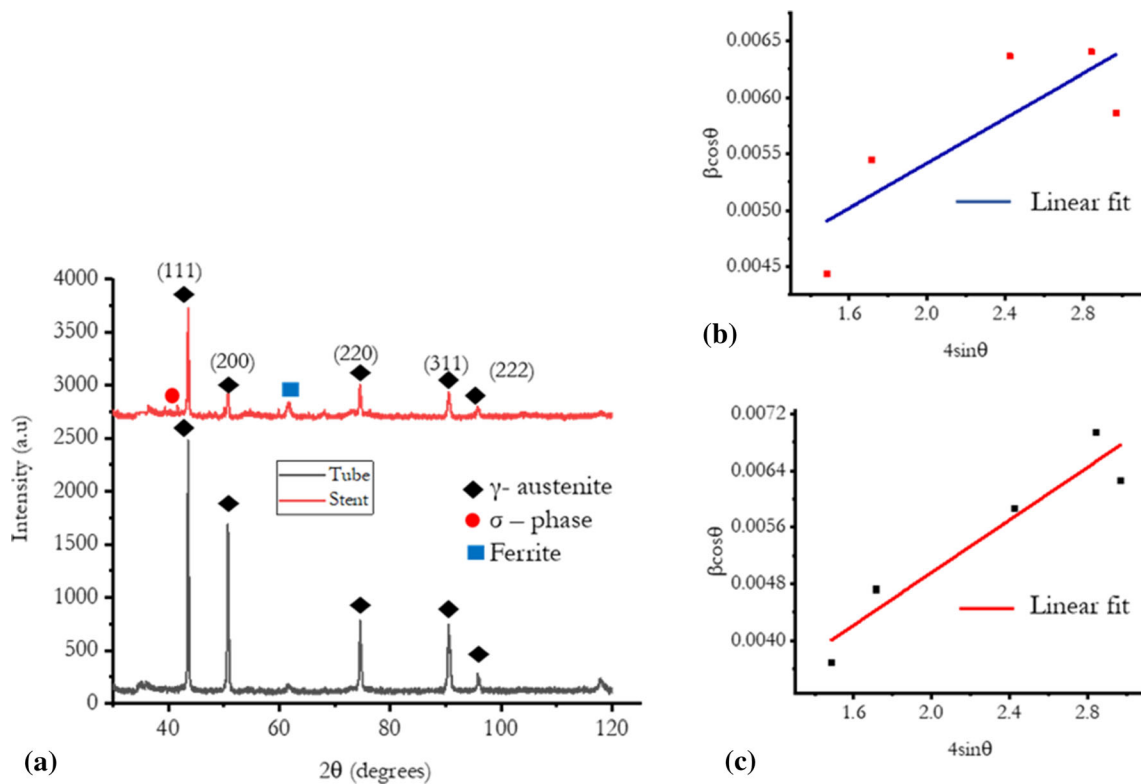**Fig. 2** (a) and (b) Surface morphology; (c) and (d) 2D surface profiles for tube and stent

Fig. 3 (a) X-ray diffraction intensity versus 2θ plot for tube and stent; (b) and (c) Williamson–Hall plots for diffraction patterns
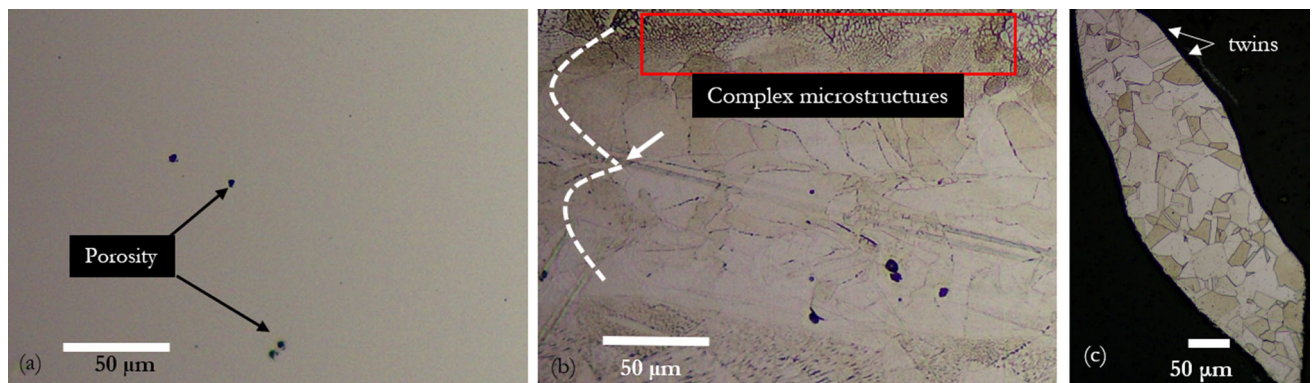

Fig. 4 (a) Optical micrograph of tube showing pore; (b) melt pool boundaries (dotted white lines) and complex microstructures toward the edges; (c) optical micrograph of stent with equiaxed grains and twins

3.3 Microstructure Characterization

3.3.1 Optical Microscopy and SEM. The optical micrograph for a polished tube demonstrated minimal porosity (Fig. 4a). The presence of pores can have a negative influence on the mechanical properties of the tube. Brooks et al. (Ref 28) and Khairallah et al. (Ref 29) showed that a lack of fusion, entrapment of gases during manufacturing, un-melted or partially melted particles and delamination between deposited layers can lead to the formation of pores. Therefore, it is important to continuously improve process parameters to minimize such defects. The etched cross section of the tube reveals the presence of hierarchical structures at macro- and micro-scales (Fig. 4b). At the macro-scale, the laser beam generated melt pool boundaries and melt traces, with structures like that of a laser weld. The melt pool was larger than 100 μm in size, as seen in the middle of the sample. The melt pools partly overlapped with each other and formed intersection points (white arrow). The size of the melt pool is affected by the process parameters used during the SLM process, which in turn affects the microstructures (Ref 30). Also, elongated grains are visible in the etched sample, they grew in the longitudinal direction. The microstructures toward the edges of the samples were very complex, as also observed in other studies (Ref 31–34). On the other hand, the optical micrograph of the etched stent (Fig. 4c) does not show the complex microstructures observed for the printed tube. The stent had instead equiaxed grains and a presence of twins.

The complex nature of the microstructure of the tube toward the edges was revealed more clearly with the help of SEM
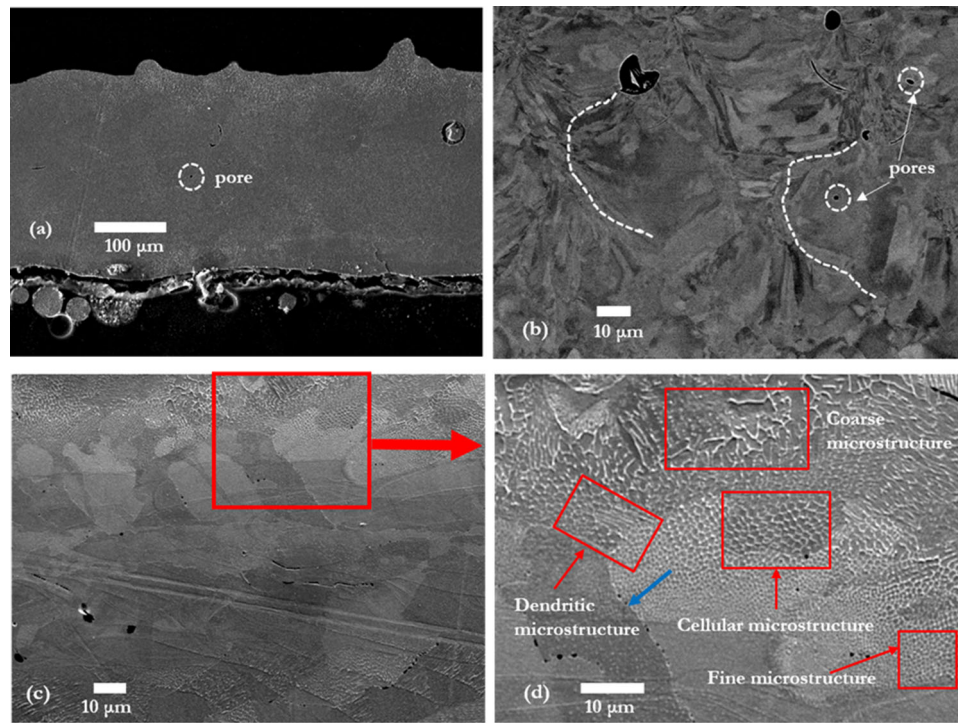
Fig. 5 (a) SEM image of tube with minimal pores; (b) backscatter secondary electron image revealing pores and melt pool boundaries; (c) SEM image of etched tube showing complex microstructures near edges; (d) higher resolution SEM image demonstrating microstructural details such as fine, coarse and dendritic structures, grain boundary (blue arrow) and cellular microstructures (Color figure online)

(Fig. 5). The SEM image of the polished sample demonstrated minimal internal pores and melt pool boundaries (Fig. 5a, b). The SEM image of the etched sample (Fig. 5c) revealed elongated grains and complex microstructures as those observed with the optical microscopy. Higher magnification SEM images showed the existence of sub-grain boundaries with different morphologies, i.e., fine and coarse, cellular and dendritic (Fig. 5d). The grain boundaries were visible, demonstrating grain variation in the size and shape. Studies (Ref 28, 35) showed that the changes in the microstructures were due to the variations in the temperature gradient (G) of the liquid–solid interface and the solidification growth rate (R). The G/R ratio determines the solidification mode such as cellular, columnar dendrite or equiaxed dendrite while the product of $G \times R$ (cooling rate) determines the size of the microstructure. A relatively high G/R ratio promotes the formation of cellular structures. The cooling rate toward the edges was higher than that in the middle of the sample, and, as a result, the finer microstructure was achieved in the former area. Furthermore, the found light cell or dendritic boundaries (Fig. 5d) are solidification sub-grain boundaries also observed by Mukherjee et al. (Ref 32). The sub-grains arise due to compositional variations caused by solute redistribution to the boundaries during solidification of austenitic stainless steel.

The chemical composition and phases of the tube and stent were thoroughly analyzed next, and the SEM/EDS analyses revealed their similar chemical composition. As evidenced by Table 1, Fe, Cr and Ni were the main alloying elements, while C, Mo, Mn and Si were the secondary elements. Still, some differences in the weight fraction of alloy elements could affect the microstructures and mechanical properties.

Table 1 EDS chemical composition of tube and stent

Specimen	Cr	Ni	C	Mo	Mn	Si	Fe
Tube	17.5	12.5	0.03	2.6	1.3	0.9	Bal
Stent	17.9	13.4	0.03	2.7	…	0.6	Bal.

3.3.2 EBSD Analyses. The EBSD inverse pole figure (IPF) maps for the tube and stent demonstrate that most of the grains had high-angle grain boundaries (Fig. 6): blue lines outline the boundaries with misorientation angles greater than 15 degrees. For the tube, the microstructure consisted of fine grains toward the edges and coarse grains at the middle. The coarse grains, with a size of hundreds of microns, were elongated in the longitudinal direction. The long axis of the grains was several hundreds of microns, even larger than the melt pool depth discussed in "Optical Microscopy and SEM" section. There were also small grains between the layers oriented in different directions. So, there was a spread in grain size, even though the larger grains were dominant. The EBSD data showed that AM resulted in non-conventional grain shape, orientation and size also reported in other studies (Ref 21, 33, 35, 36). The average grain size for the tube along the longitudinal cross section was 72.15 μm. IPFs also showed a continuous change in color within most grains, reflecting a continuous variation in the orientation. It can also suggest the presence of significant dislocation substructures. It was also observed that the phase of the as-built tube was almost pure austenite, which agrees with XRD results in "Composition and Phases" section.

On the other hand, the stent with an average grain size of 20 μm (Fig. 6 (c) and (d)) was formed by homogenously
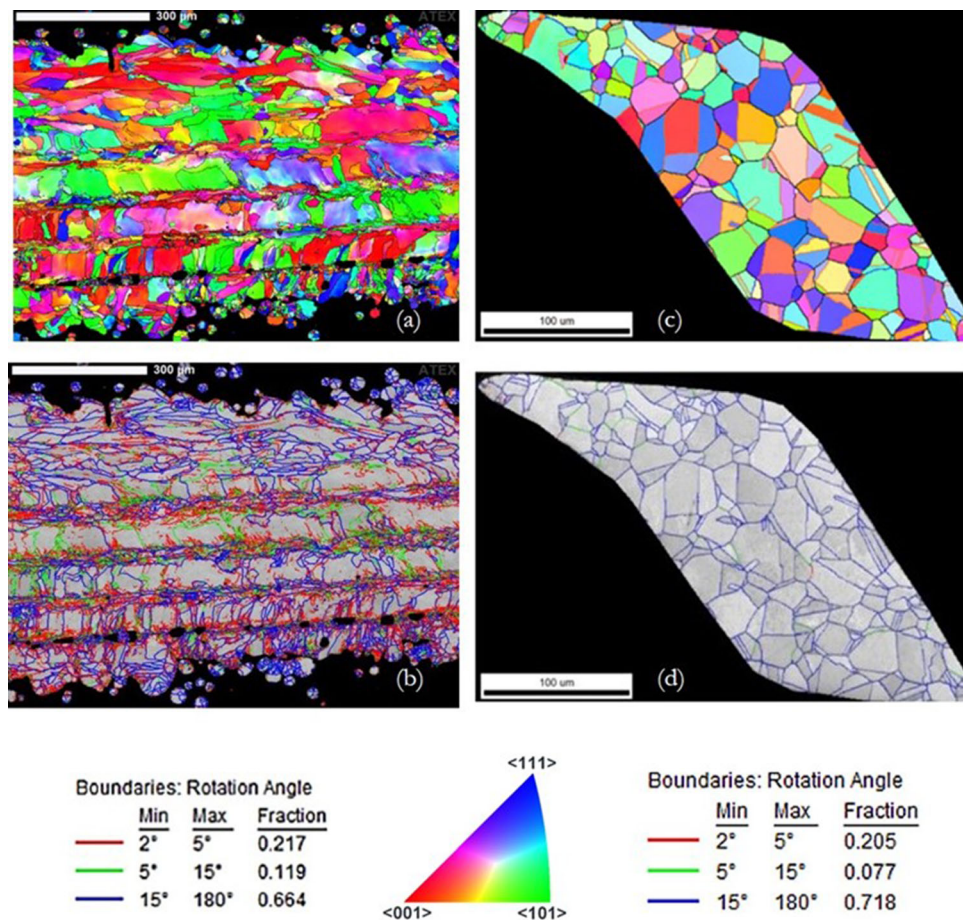
Fig. 6 EBSD inverse pole figure maps and grain boundary character for (a) and (b) tube and (c) and (d) stent in longitudinal cross-sections

distributed equiaxed fine grains. Apparently, the stent had only a few grains across its width due to their size. Further, the stent sample had twins in its microstructure, suggesting that heat treatment was performed. Other studies (Ref 37, 38) also showed equiaxed grains and twining in 316L SS as a result of grain recrystallisation during the heat treatment process.

3.4 Nanoindentation Testing

3.4.1 Berkovich Nanoindentation. The load–displacement responses obtained from Berkovich nanoindentation at 3, 7, 10, 15 and 25 mN are consistent each load. It is also evident from the plots that, even at very low loads, the samples exhibited very little strain recovery, indicating severe plastic deformation under Berkovich nanoindentation.

The Young's modulus and hardness at each load were calculated using the Oliver and Pharr method as discussed in "Berkovich Nanoindentation" section and compared for the samples (Fig. 7). The tube exhibited the hardness in the range of 3.2–3.8 GPa and the Young's modulus of 207–227 GPa. On the other hand, the hardness and elastic modulus for the stent were in the range 2.3–3.2 and 120–180 GPa, respectively. Apparently, the hardness of the tube was much higher compared to that of the stent. The higher value of hardness for the tube was the result of the greater fragmentation of the microstructure, which increased the dislocation density and internal strain in the AM tube. The H and E values reduced with

increasing load due to the indentation size effect, but not much (Fig. 7c, d).

A spread in the load–displacement curves for indents made at the same load (Fig. 7) suggests that the mechanical response was different. To investigate the effect of grain orientation on hardness and Young's modulus, EBSD analyses were performed for 4×4 indents made on selected grains at 7 and 25 mN for the SLMed tube (Fig. 8a, b). The black triangles indicate the locations of indents.

Four indents were selected at each load, with two in the same grains. For the indent at 7 mN, two grains were with relatively similar orientation (shown in pink and blue in Fig. 8a). Similarly, for indents made at 25 mN two grains also had a similar orientation (shown in pink and blue in Fig. 8b). The initial stage of the load-depth response coincided for all the four imprints in each case, implying similar mechanical behavior of the sample within the elastic region. The difference in the load–displacement curves were observed at the elastic–plastic transition; they kept increasing up to peak load. Still, the responses for the imprints on the grain with a similar orientation were consistent with each other. At the same load level, deeper penetration was achieved for the indents in purple grains compared to those in the blue grains. For all the indentation points, orientation in terms of Bunge–Euler angles was extracted using the HKL Channel 5.0 EBSD postprocessing software. Further, the hardness and Young's modulus were calculated for each indentation point. Table 2 gives a summary
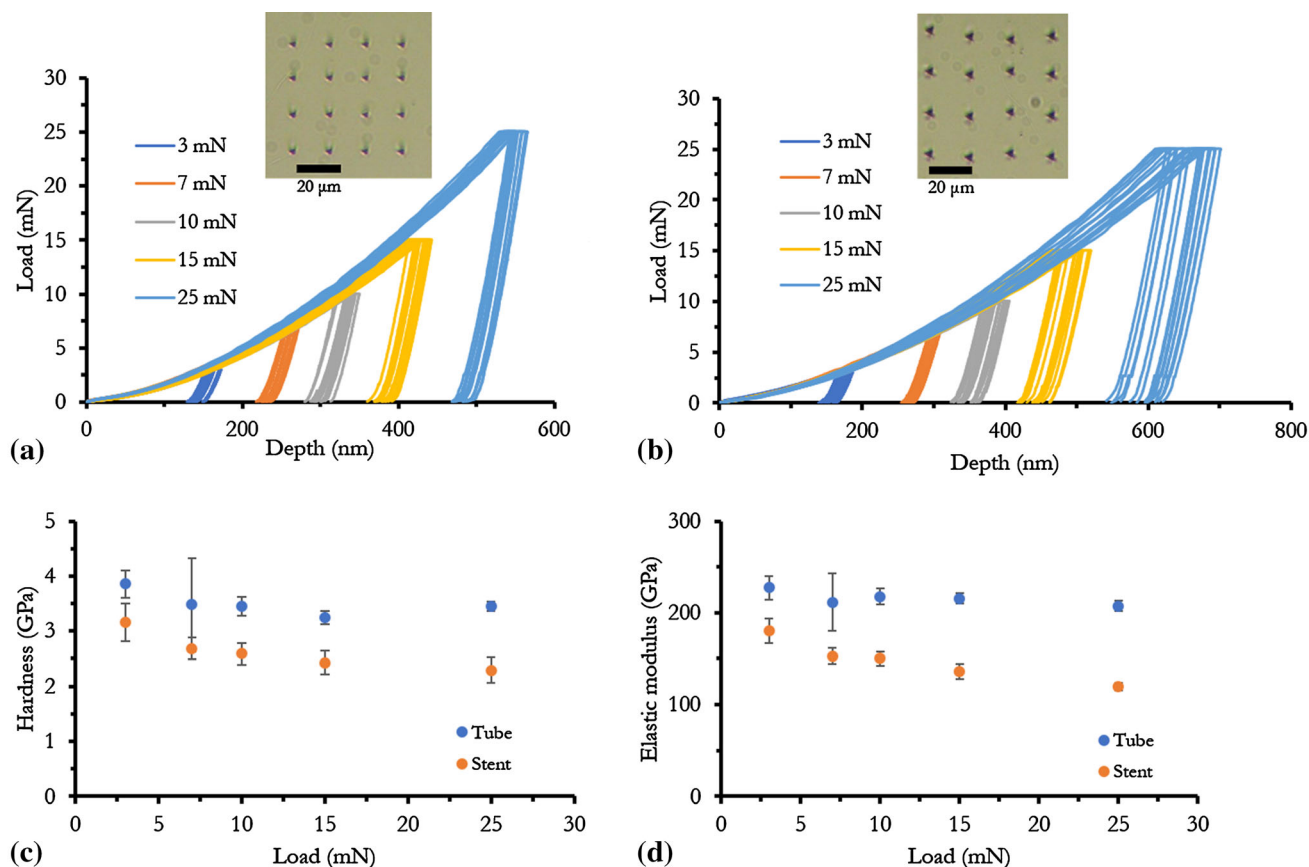
Fig. 7 (a) and (b) Representative load–displacement curves. The inset shows 4 × 4 indentation imprint. Variation in (c) hardness and (d) Young's modulus at different load levels for tube and stent

of the extracted Bunge–Euler orientation angle, calculated hardness and the Young's modulus for the tube.

For the indents performed at 7 mN, in the grains close to (111), the hardness was 3.8–4.0 GPa, and Young's modulus in the range 229.4–236.0 GPa. On the other hand, for grains close to (001) the hardness was in the range 3.6–3.9 GPa and Young's modulus in the range 210.0–228.0 GPa. The hardness and the Young's modulus values calculated for AM were higher than that of 316L SS materials produced via conventional routes (Ref 39). The results for the Young's modulus and hardness plotted in the standard stereographic triangles (SST) (Fig. 9) show that they were affected by grain orientation. They had strong anisotropy depending on the crystallographic orientation: grains close to (111) had the higher Young's modulus and hardness than those close to (001) Similar results were also found for the commercial stent which are omitted here to avoid duplications.

Nanoindentation tests were also conducted on the surface, longitudinal and radial cross sections to compare the hardness and elastic modulus. Figure 10(a) and (b) shows hardness and the elastic modulus results. As can be seen, the hardness and elastic modulus taken in the longitudinal and radial cross sections gave consistent results while a large scattering was seen for the surface. There was also a significant difference in the hardness between surface layer and the core of thin-walled tube. This is caused by the surface roughness as well as variation of microstructures linked with the SLM process, suggesting surface polishing process will be required for stent application.

3.4.2 Spherical Nanoindentation. Spherical nanoindentation was performed on the tube and stent to assess their yield strength and hardening behavior, besides hardness and the Young's modulus obtained with Berkovich nanoindentation. Here, twenty loading and unloading nanoindentation cycles were performed with a minimum and maximum load of 1 and 50 mN, respectively. The indents were nearly spherical (Fig. 11), and no cracks were observed around them at these load levels. It is evident from the load–displacement graphs that the loading–unloading behavior captured with spherical nanoindentation was consistent for all the indents. The maximum indentation depth was found to be 406.36 nm for the tube and 480.24 nm for the stent. Apparently, all the samples experienced significant plastic deformation with very little elastic recovery.

The method proposed by Kalidindi et al. (Ref 22) was used to extract the indentation stress–strain curve from the load–displacement response. It involved the identification of the effective initial contact and determination of the contact radius. Two observation can be made from the representative indentation stress–strain curves shown in Fig. 12. First, they demonstrate good consistency within the elastic region and an increased scatter in the plastic region. Second, the indentation stress–strain response was similar for the tube and the stent, showing that the material was hardened to a similar level despite differences in the initial microstructure. On the other hand, AM material exhibited a bulk compression yield stress ~ 60% higher than that obtained in conventional manufacturing with similar work hardening (Ref 40). The increase in the

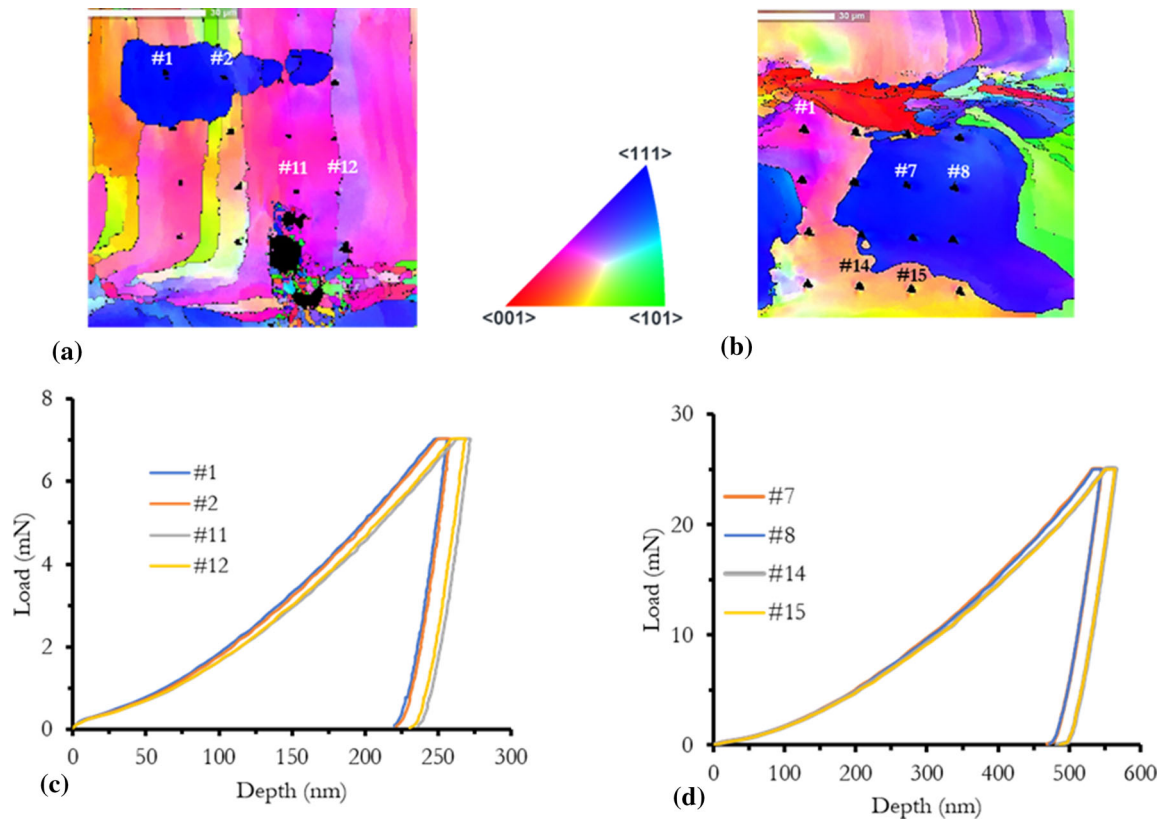**Fig. 8** EBSD IPF maps for imprints made at (a) 7 mN and (b) 25 mN, together with corresponding load–displacement curves for (c) 7 mN and (d) 25 mN

Table 2 Summary of Bunge–Euler orientation angles (in degrees), hardness and Young's modulus for indents in tube at 7 and 25 mN

Indent #	7 mN			25 mN		
	Orientation $\varphi_1, \Phi, \varphi_2$	H, GPa	E, GPa	Orientation $\varphi_1, \Phi, \varphi_2$	H, GPa	E, GPa
#1	354.78, 29.55, 80.09	4.01	236.04	312.23, 30.83, 61.98	3.45	210.88
#2	333.24, 28.80, 6.76	3.94	234.11	306.51, 24.09, 70.79	3.48	213.33
#3	340.67, 26.90, 3.51	3.80	235.67	309.01, 23.07, 68.44	3.55	209.39
#4	132.31, 25.34, 50.77	3.83	229.41	303.65, 24.99, 73.54	3.55	211.48
#5	112.79, 21.43, 73.16	3.79	227.96	316.14, 23.44, 61.9	3.36	211.40
#6	106.31, 20.54, 72.09	3.76	226.24	333.86, 49.98, 43.53	3.37	216.19
#7	121.96, 31.92, 60.30	3.56	220.08	335.8, 46.91, 43.23	3.46	206.56
#8	121.98, 32.56, 60.91	4.12	210.43	334.11, 44.83, 41.96	3.48	204.10
#9	114.86, 27.47, 73.15	3.86	223.79	332.86, 28.03, 37.81	3.46	211.44
#10	114.81, 22.62, 69.07	3.80	218.09	313.27, 28.16, 62.28	3.49	213.82
#11	122.81, 31.38, 58.93	3.59	219.26	333.58, 48.15, 41.09	3.60	200.91
#12	131.08, 30.48, 60.30	3.67	213.70	335.98, 44.26, 36.97	3.55	204.84
#13	115.58, 25.27, 71.89	1.26	135.75	332.84, 23.14, 35.91	3.33	197.12
#14	121.82, 14.33, 59.50	1.46	130.72	315.63, 25.45, 60.55	3.31	199.57
#15	125.75, 32.20, 55.63	3.61	210.02	346.14, 43.66, 34.54	3.31	202.84
#16	129.13, 30.93, 53.39	3.57	213.86	340.64, 40.88, 33.49	3.46	205.40

bulk yield stress for AM was argued to come from microstructural features or deformation processes at a higher length scale than that of spherical nanoindentation tests. As reported in "EBSD Analyses" section, the average grain size for the tube and stent was 72 and 20 μm, respectively. This implied that the indents were into one to two grains for the tube and four to six grains for the stent depending on their location. Therefore, the grain size and morphology differences between the tube and the stent should not have a significant influence on the indentation stress–strain measurements. Further, the complex microstructures observed in the tube did not appear to influence the indentation stress–strain curve. Third, the strain value for the
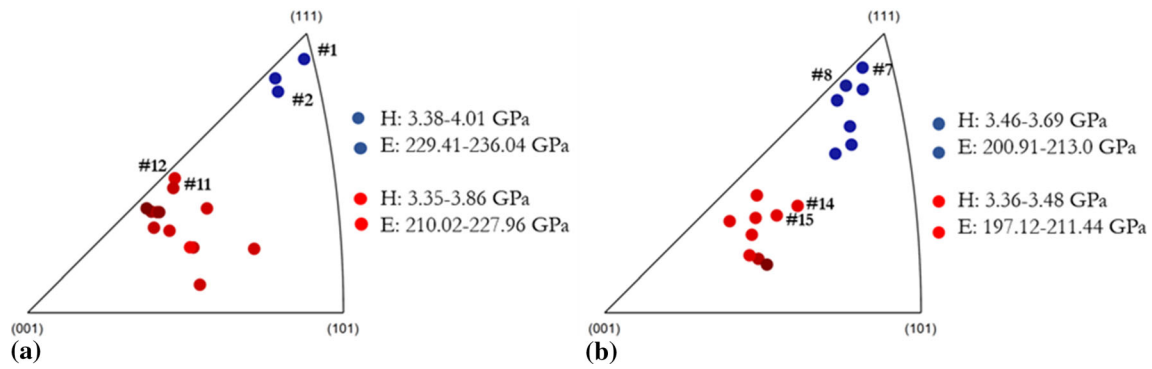
Fig. 9 Hardness and Young's modulus of tube on SST for nanoindentation performed at (a) 7 mN and (b) 25 mN
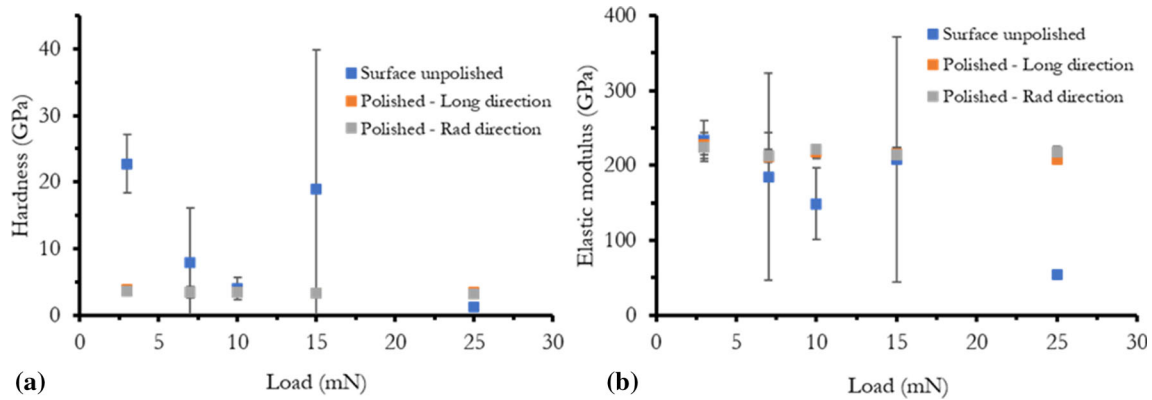

Fig. 10 Variation in (a) hardness and (b) elastic modulus on the surface, longitudinal and radial directions at different load levels for tube
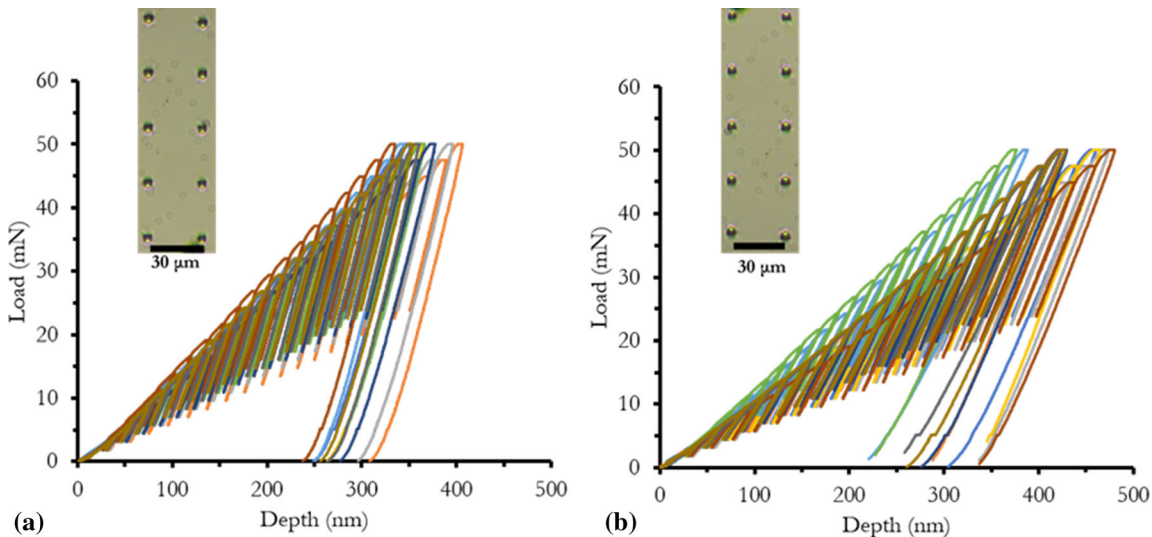

Fig. 11 Load-displacement curves for (a) tube and (b) stent

stent was higher than that of the AM sample. Table 3 gives a summary of the Young's modulus and yield strength extracted from indentation stress–strain curves.

The Young's modulus for the AM sample and the commercial stent was 198.9 ± 9.22 and 190.3 ± 3.13 GPa while the yield strength was 2.2 ± 0.30 and 2.0 ± 0.24 GPa, respectively. The magnitude of yield strength was significantly higher than that obtained from the uniaxial tensile test of AM 316L SS as reported by Yin et al. (Ref 21). According to the

measurements, the nanoindentation yield strength was nearly 3.4 times that measured from uniaxial tensile tests. As suggested by Pathak and Kalidindi (Ref 41), a factor is thus required to correlate the uniaxial and nanoindentation stress state: $\sigma = \sigma_{ind}/\delta$, where σ is uniaxial stress, σ_{ind} is the nanoindentation stress and δ is the correlation factor. By applying the correlation factor, the indentation yield strength can more closely match the uniaxial tensile yield strength value.
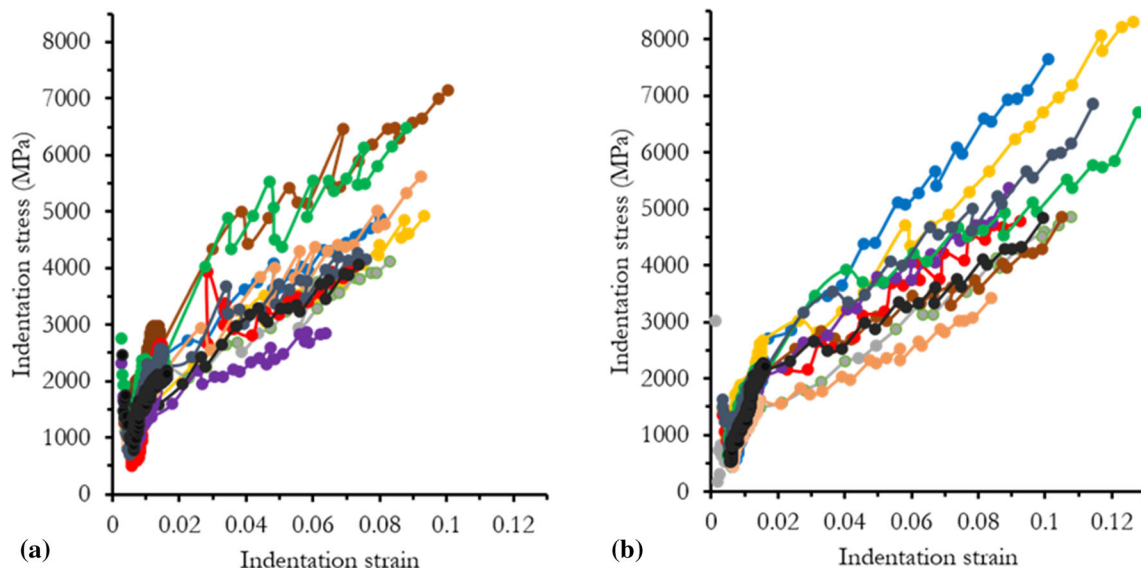
Fig. 12 Indentation stress–strain curves for (a) tube and (b) stent

Table 3 Young's modulus and yield strength obtained from nanoindentation

	Tube		Stent	
Indent #	E_{ind}, GPa	Y_{ind}, MPa	E_{ind}, GPa	Y_{ind}, MPa
#1	198.3	2486.3	187.7	2486.3
#2	206.4	1592.5	191.3	2020.0
#3	184.0	2215.0	186.9	1863.2
#4	205.1	2231.6	195.2	1760.0
#5	190.3	2669.3	189.2	1920.4
#6	206.3	1991.1	193.5	2160.2
#7	211.7	2178.7	194.1	1630.9
#8	199.8	2358.3	186.7	1960.3
#9	200.8	2248.6	190.0	2020.1
#10	186.6	1931.8	187.9	2200.0

The Young's modulus obtained for the stent matched well with the reported standard 316L SS. This suggests that the mechanical properties of the samples were accurately captured within the elastic region. The stress–strain curves for the tube and stent were further fitted to the Ramberg–Osgood relationship (Fig. 13a, b) $\frac{\varepsilon}{\varepsilon_0} = \frac{\sigma}{\sigma_0} + \alpha \left(\frac{\sigma}{\sigma_0} \right)^n$, where ε is the total strain, ε_0 is the strain at the yield point, σ is the total stress, σ_0 is the yield stress, α is the non-dimensional material constant and n is the strain hardening exponent. Such fitting of representative average stress–strain curves for the two samples resulted in the strain hardening exponent, 4.2 and 3.8, respectively, for the tube and stent.

4. Discussion

AM is a maturing technology which has been attempted to produce polymeric and metallic stents. However, the full potential of producing metallic stents is an ongoing endeavor. Although studies on microstructural and mechanical characterization of AM metallic materials is well established for use in some medical devices such as orthopedic implants, dental devices, no comprehensive work has been dedicated to studying metallic stents produced with SLM, especially the microstructures and its connection with mechanical properties. In this work, a thin-walled tube was fabricated as a first step in understanding microstructural and mechanical properties of SLMed samples for stent application. Actual stent has a much smaller structural size ($\sim$ 75–100 μm strut size), presenting a huge challenge for SLM in terms of providing their structural integrity, as stents are designed for load bearing purposes. Through the pilot studies on SLMed tubes, we aim to investigate the feasibility of SLM for stent manufacturing in terms of microstructure and mechanical properties as well as powder preparation and the additive process. The manufacturing of tube as feedstock for stent micromachining may be slightly more expensive and material wasting, but it is still economic compared to conventional tube production through drawing process and also can serve as a viable alternative technique for stent manufacturing. AM of commercial types of stent still represents a huge challenge at the moment due to the extremely thin strut size and also the open-cell design which cannot be produced via SLM as a result of lack of material support during the SLM process.

The results of this study indicated that the microstructures and mechanical properties were affected by the SLM process. In normal operation, stents should be able to withstand cyclic pulsation from the artery, so fatigue properties should be adequate. It is preferred for the stent to have a number of equiaxed grains (e.g., size of 5–10 μm) across its width. However, the fast cooling and layer by layer of the powder resulted in coarse and columnar grains in the middle of the wall with complex microstructures toward the edges. Further, the surface quality of the tube can be an issue for fatigue properties. To improve fatigue resistance, surface defects and internal pores should be kept minimal (Ref 42). Recently, computational and experimental studies were performed to investigate the effect of melting modes (conduction, transition and keyhole) on 316L SS parts fabricated by SLM (Ref 43, 44). Results showed that a stable free keyhole melting mode of 316L SS produced porosity-free single-track deposition with
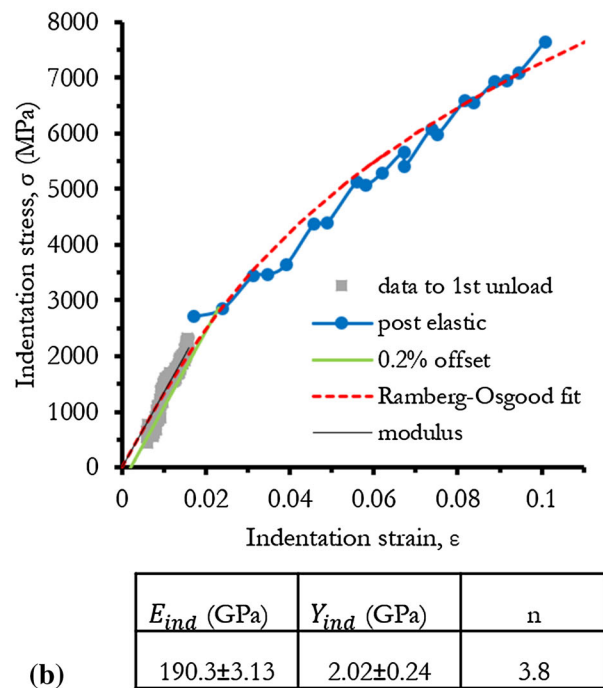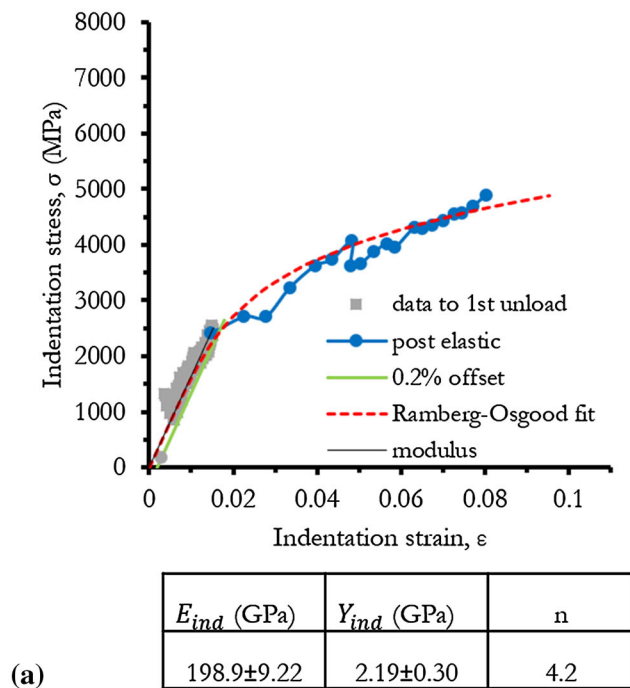
E_{ind} (GPa)	Y_{ind} (GPa)	n
198.9±9.22	2.19±0.30	4.2

(a)

E_{ind} (GPa)	Y_{ind} (GPa)	n
190.3±3.13	2.02±0.24	3.8

(b)

Fig. 13 Spherical nanoindentation stress–strain curves for (a) tube and (b) stent, showing indentation modulus, E_{ind}, yield stress defined by 0.2% indentation strain offset and Ramberg–Osgood fit

finer grains (0.28 μm cellular spacing) and substantially higher nanohardness and elongation to failure.

The SLMed tube had an average area porosity of less than 1% in the optimum condition. In this study and also other published work (Ref 28, 29), it was difficult to totally eliminate the porosity in SLM due to the stochastic phenomena that happen during the manufacturing process. In general, the porosity may compromise the fatigue behavior of the material (Ref 45). The pores reduce the time to crack initiation by creating a high stress concentration region adjacent to this microstructural defect. Generally, the presence of pores does not affect the strength and ductility of the SLMed samples when the porosity is less than 1 vol.% (Ref 46). However, when the pores have a relatively big size (in the range of 15 to 600 μm) and irregular morphology, they cause detrimental effect to the mechanical properties (lowering ductility and strength) due to sharp features which act as stress concentrations (Ref 47, 48). Nonetheless, the strength of SLMed samples, especially stainless steels, is compensated by the presence of the fine cellular microstructure and the dislocation networks formed during the rapid cooling in the manufacturing process. Dislocation motion in SLMed 316L SS can be hindered, but not fully stopped, by dislocation networks formed in the material (see Fig. 5d). When load is applied to a sample with dislocation network, the major carriers of plastic deformation are partial dislocations whose motion can be significantly, but not completely, impeded by the dislocation networks. The partial dislocations are temporally trapped in the dislocation walls but can move forward again with the increase in stress. Consequently, the impediment effect of the complex dislocation networks leads to increased strength and ductility in SLMed 316L SS (Ref 49).

The surface quality of the SLMed tube can be problematic for fatigue properties and internal pores and surface defects should be kept minimal. Our results showed that the printed

tube had minimal internal defects; however the surface quality should be improved for fatigue resistance. Mechanical surface treatments such as laser shock peening (LSP) (Ref 50), shot peening (SP) (Ref 51), ultrasonic shot peening (USP) (Ref 52), ultrasonic impact treatment (UIT) (Ref 53) and barrel finishing (BF) (Ref 54) can be very effective by eliminating residual porosities (see Fig. 4, 5), especially in the near-surface layers. For instance, LSP uses a high-energy pulsed laser to generate severe plastic deformation at the surface of the sample. On the contrary, other processes consist of directional (SP) or random (BF or USP) striking an area of the surface by high-energy balls. The UIT process involves severe plastic deformation of the surface by multiple impactions with several cylindrical pins. All these modifications of the near-surface layers can lead to surface microrelief, compressive residual macro-stress and increased surface hardness. In addition, the surface quality of the tube can be improved with the use of different post-processing methods such as chemical and electrochemical polishing (Ref 20, 55). With this method, metallic surface is smoothed (levelling micro-peaks and valleys) by polarizing it anodically in an adequate electrolyte.

In this study also, the hardness of the tube was found to be higher than that of the stent, which confirms that the microstructures affected the mechanical properties of the printed tube. Therefore, solution annealing heat treatment is required to lower the hardness (Ref 56, 57). Also, it will improve the mechanical behavior by stress relieving, improving the elongation at break and providing equiaxed grains (Ref 58). Despite a significant difference in the microstructures, indentation stress–strain curves for the tube and stent were comparable. The argument for this is as follows. The volume of material probed during spherical indentation was estimated as a cylinder with a radius equal to the contact radius and height 2.4 multiplied by the contact radius (Ref 23). At the yield point, the contact radius was $\sim$ 250 nm with a 10 μm spherical tip

radius. We have reported that the grain size for the tube and stent were 72 and 20 μm, respectively. This implied that most of the indents were probing within the grain with some on the grain boundary depending on where the indents were placed. Therefore, the grain size and morphology did not have a significant effect on the extracted indentation stress–strain curve and the yield strength through spherical nanoindentation. However, further mechanical tests such as tensile and fatigue experiments at sample level are under way to gain a more thorough understanding of the effect of grain microstructure on the stress–strain response of SLMed thin-walled structure.

Fabrication of stents has been pursued through a variety of schemes such as laser cutting, photo etching, electroforming, micro-electro-discharge machining, molding and casting (Ref 59). The multitude of fabrication modalities has resulted from a divergent set of materials used to develop stent platforms as well as advanced design considerations. It is particularly noted that the latest and novel AM technology has enabled a rapid and parallel generation of complex 3-dimensional structures with intrinsic geometric freedom, dimension variability and extensive saving of raw materials. AM via SLM offers the most promising approach to generate vascular scaffolds with customized designs compared to conventional stent manufacturing techniques. However, one of the major technical hurdles for AM of stents is the considerable lack of strength in the fabrication direction, which essentially prevents proper functioning of the devices. This could be due to the non-uniform melting process of the powders during the SLM process. Another urgent and unresolved issue is the lack of sustainable plastic deformation, which may cause the fracture of stents during and post-implantation, leading to a failure of the surgery process and clinical complications (Ref 60). Consequently, critical developments are required to increase the strength, ductility and toughness of devices made with the SLM process. These devices are designed for load-bearing purposes but have a much smaller structural size (below 100 μm), presenting a huge challenge for AM in terms of providing their structural integrity. This paper provides a study of microstructures and mechanical behavior of AM thin-walled tube in comparison with the commercial stent, which is helpful for the adoption of AM for stent production. The results of this study suggest that grain microstructure of SLMed tube will need to be optimized, for instance through heat treatment, to further improve the mechanical properties required for stents (e.g., both strength and ductility). It is also necessary to further reduce the tube wall thickness (currently $\sim$ 500 μm; five times thicker than commercial ones) during SLM process in future research, in order to match the thin strut structure of commercial stents (minimizing the negative impact on hemodynamic after stent implantation). Overall, the current work is a step forward toward manufacturing of stents via AM, seen as a breakthrough in development of personalized therapy.

5. Conclusions

In this study, the microstructures and mechanical properties of the stainless steel tube and the stent were investigated using EBSD and nanoindentation. The findings are:

- The surface roughness for the tube was higher than that of the stent. Therefore, surface treatment process is re-

quired for the tube in order to meet the surface finish recommended for stents.
- The chemical composition of the tube was similar to that of the stent, but with some differences in weight fractions of alloy elements. Both samples were fully austenitic without traces of the second phase.
- Microscopy characterization revealed different microstructures of the tube and the stent. The former had a dominant coarse and columnar grain structure in the middle of the wall with complex microstructures toward the edges, as opposed to equiaxed fine grains in the stent.
- Despite significant differences in the microstructures between the tube and the stent, indentation stress–strain curves were close to each other. Berkovich nanoindentation indicated that grain orientation affected the hardness and the Young's modulus of the materials, with the indents close to (111) planes exhibiting the highest levels of hardness and elastic modulus.
- The results of this study suggest that grain microstructure of SLMed tube can be further optimized to improve the mechanical properties required for stents. Also, the tube wall thickness can be further reduced during SLM in order to match the thin strut structure of commercial stents.

References

1. World Health Organisation, "Cardiovascular Diseases (CVDs)," 2017, https://www.who.int/en/news-room/fact-sheets/detail/cardiovascular-diseases-(cvds). Accessed 21 Aug 2020
2. C. Bauters, T. Meurice, M. Hamon, E. McFadden, J.M. Lablanche, and M.E. Bertrand, Mechanisms and Prevention of Restenosis: From Experimental Models to Clinical Practice, *Cardiovasc. Res.*, 1996, **31**(6), p 835–846

3. D.L. Fischman, M.B. Leon, D.S. Baim, R.A. Schatz, M.P. Savage, I. Penn, K. Detre, L. Veltri, D. Ricci, M. Nobuyoshi, M. Cleman, R. Heuser, D. Almond, P.S Teirstein, D. Fish, A. Colombo, J. Brinker, J. Moses, A. Shaknovich, J. Hirshfeld, S. Bailey, S. Ellis, R. Rake, and S. Goldberg, A Randomized Comparison of Coronary-Stent Placement and Balloon Angioplasty in the Treatment of Coronary Artery Disease, *N. Engl. J. Med.*, 1994, **331**(8), p 496–501

4. P.W. Serruys, P. de Jaegere, F. Kiemeneij, C. Macaya, W. Rutsch, G. Heyndrickx, H. Emanuelsson, J. Marco, V. Legrand, P. Materne, J. Belardi, U. Sigwart, A. Colombo, J.J. Goy, P. van den Heuvel, J. Delcan, and M. Morel, A Comparison of Balloon-Expandable-Stent Implantation with Balloon Angioplasty in Patients with Coronary Artery Disease, *N. Engl. J. Med.*, 1994, **331**(8), p 489–495

5. J.W. Moses, M.B. Leon, J.J. Popma, P.J. Fitzgerald, D.R. Holmes, C. O'Shaughnessy, R.P. Caputo, D.J. Kereiakes, D.O. Williams, P.S. Teirstein, J.L. Jaeger, and R.E. Kuntz, Sirolimus-Eluting Stents versus Standard Stents in Patients with Stenosis in a Native Coronary Artery, *N. Engl. J. Med.*, 2003, **349**, p 1315–1323

6. C. Stettler, S. Wandel, S. Allemann, A. Kastrati, M.C. Morice, A. Schömig, M.E. Pfisterer, G.W. Stone, and M.B. Leon, Outcomes Associated with Drug-Eluting and Bare-Metal Stents: A Collaborative Network Meta-Analysis, *Lancet*, 2007, **370**(9591), p 937–948

7. R. Erbel, C. Di Mario, J. Bartunek, J. Bonnier, B. de Bruyne, F.R. Eberli, P. Erne, M. Haude, B. Heublein, M. Horrigan, C. Ilsley, D. Böse, J. Koolen, T.F. Lüscher, N. Weissman, and R. Waksman, Temporary Scaffolding of Coronary Arteries with Bioabsorbable Magnesium Stents: A Prospective, Non-Randomised Multicentre Trial, *Lancet*, 2007, **369**(9576), p 1869–1875

8. Eurostat, "Cardiovascular Diseases Statistics—Statistics Explained," 2019, https://ec.europa.eu/eurostat/statistics-explained/index.php?title=Cardiovascular_diseases_statistics#Cardiovascular_healthcare. Accessed 21 Aug 2020

9. A.C. Morton, D. Crossman, and J. Gunn, The Influence of Physical Stent Parameters upon Restenosis, *Pathol. Biol.*, 2004, **52**(4), p 196–205

10. H. Hara, M. Nakamura, J.C. Palmaz, and R.S. Schwartz, Role of Stent Design and Coatings on Restenosis and Thrombosis, *Adv. Drug Deliv. Rev.*, 2006, **58**(3), p 377–386

11. N. Muhammad, D. Whitehead, A. Boor, and L. Li, Comparison of Dry and Wet Fibre Laser Profile Cutting of Thin 316L Stainless Steel Tubes for Medical Device Applications, *J. Mater. Process. Technol.*, 2010, **210**(15), p 2261–2267

12. R.T. Lee, A.J. Grodzinsky, E.H. Frank, R.D. Kamm, and F.J. Schoen, Structure-Dependent Dynamic Mechanical Behavior of Fibrous Caps from Human Atherosclerotic Plaques, *Circulation*, 1991, **83**(5), p 1764–1770

13. J.E. Roos, J.C. Hellinger, R. Hallet, D. Fleischmann, C.K. Zarins, and G.D. Rubin, Detection of Endograft Fractures with Multidetector Row Computed Tomography, *J. Vasc. Surg.*, 2005, **42**(5), p 1002–1006

14. T.D. Ngo, A. Kashani, G. Imbalzano, K.T.Q. Nguyen, and D. Hui, Additive Manufacturing (3D Printing): A Review of Materials, Methods, Applications and Challenges, *Compos. Part B Eng.*, 2018, **143**, p 172–196

15. M. Centola, A. Rainer, C. Spadaccio, S. De Porcellinis, J.A. Genovese, and M. Trombetta, Combining Electrospinning and Fused Deposition Modeling for the Fabrication of a Hybrid Vascular Graft, *Biofabrication*, 2010, **2**(1), p 1–11

16. S.S. Moore, K.J. O'Sullivan, and F. Verdecchia, Shrinking the Supply Chain for Implantable Coronary Stent Devices, *Ann. Biomed. Eng.*, 2016, **44**(2), p 497–507

17. Food & Drug Administration, "UPDATE on Increased Rate of Major Adverse Cardiac Events Observed in Patients Receiving Abbott Vascular's Absorb GT1 Bioresorbable Vascular Scaffold (BVS)—Letter to Health Care Providers | FDA," 2018, https://www.fda.gov/medical-devices/letters-health-care-providers/update-increased-rate-major-adverse-cardiac-events-observed-patients-receiving-abbott-vasculars. Accessed 21 Aug 2020

18. Y. Wessarges, R. Hagemann, M. Gieseke, C. Nölke, S. Kaierle, W. Schmidt, K.P. Schmitz, and H. Haferkamp, Additive Manufacturing of Vascular Implants by Selective Laser Melting, *Biomed. Tech.*, 2014, **59**(s1), p S385–S388

19. A.G. Demir and B. Previtali, Additive Manufacturing of Cardiovascular CoCr Stents by Selective Laser Melting, *Mater. Des.*, 2017, **119**, p 338–350

20. V. Finazzi, A.G. Demir, C.A. Biffi, F. Migliavacca, L. Petrini, and B. Previtali, Design and Functional Testing of a Novel Balloon-Expandable Cardiovascular Stent in CoCr Alloy Produced by Selective Laser Melting, *J. Manuf. Process.*, 2020, **55**, p 161–173

21. Y.J. Yin, J.Q. Sun, J. Guo, X.F. Kan, and D.C. Yang, Mechanism of High Yield Strength and Yield Ratio of 316 L Stainless Steel by Additive Manufacturing, *Mater. Sci. Eng., A*, 2019, **744**, p 773–777

22. W.C. Oliver and G.M. Pharr, An Improved Technique for Determining Hardness and Elastic Modulus Using Load and Displacement Sensing Indentation Experiments, *J. Mater. Res.*, 1992, **7**(6), p 1564–1583

23. S. Pathak and S.R. Kalidindi, Spherical Nanoindentation Stress-Strain Curves, *Mater. Sci. Eng. R Rep.*, 2015, **91**, p 1–36

24. J.S. Weaver, A. Khosravani, A. Castillo, and S.R. Kalidindi, High Throughput Exploration of Process-Property Linkages in Al-6061 Using Instrumented Spherical Microindentation and Microstructurally Graded Samples, *Integr. Mater. Manuf. Innov.*, 2016, **5**(1), p 192–211

25. A. Khosravani, A. Cecen, and S.R. Kalidindi, Development of High Throughput Assays for Establishing Process-Structure-Property Linkages in Multiphase Polycrystalline Metals: Application to Dual-Phase Steels, *Acta Mater.*, 2017, **123**, p 55–69

26. M. Shamsujjoha, S.R. Agnew, J.M. Fitz-Gerald, W.R. Moore, and T.A. Newman, High Strength and Ductility of Additively Manufactured 316L Stainless Steel Explained, *Metall. Mater. Trans. A Phys. Metall. Mater. Sci.*, 2018, **49**(7), p 3011–3027

27. K. Saeidi, X. Gao, F. Lofaj, L. Kvetková, and Z.J. Shen, Transformation of Austenite to Duplex Austenite-Ferrite Assembly in Annealed Stainless Steel 316L Consolidated by Laser Melting, *J. Alloys Compd.*, 2015, **633**, p 463–469

28. J.W. Brooks, C. Qiu, M.M. Attallah, C. Panwisawas, M. Ward, and H.C. Basoalto, On the Role of Melt Flow into the Surface Structure and Porosity Development during Selective Laser Melting, *Acta Mater.*, 2015, **96**, p 72–79

29. S.A. Khairallah, A.T. Anderson, A.M. Rubenchik, and W.E. King, Laser Powder-Bed Fusion Additive Manufacturing: Physics of Complex Melt Flow and Formation Mechanisms of Pores, Spatter, and Denudation Zones, *Addit. Manuf. Handb. Prod. Dev. Def. Ind.*, 2017, **108**, p 613–628

30. A. Leicht, M. Rashidi, U. Klement, and E. Hryha, Effect of Process Parameters on the Microstructure, Tensile Strength and Productivity of 316L Parts Produced by Laser Powder Bed Fusion, *Mater. Charact.*, 2020, **159**, p 110016

31. M. Mukherjee, Effect of Build Geometry and Orientation on Microstructure and Properties of Additively Manufactured 316L Stainless Steel by Laser Metal Deposition, *Materialia*, 2019, **7**, p 5–8

32. X. Wang, J.A. Muñiz-Lerma, O. Sánchez-Mata, M. Attarian Shandiz, and M. Brochu, Microstructure and Mechanical Properties of Stainless Steel 316L Vertical Struts Manufactured by Laser Powder Bed Fusion Process, *Mater. Sci. Eng.*, 2018, **736**, p 27–40

33. M. Godec, S. Zaefferer, B. Podgornik, M. Šinko, and E. Tchernychova, Quantitative Multiscale Correlative Microstructure Analysis of Additive Manufacturing of Stainless Steel 316L Processed by Selective Laser Melting, *Mater. Charact.*, 2020, **160**, p 1–9

34. K. Saeidi, X. Gao, Y. Zhong, and Z.J. Shen, Hardened Austenite Steel with Columnar Sub-Grain Structure Formed by Laser Melting, *Mater. Sci. Eng., A*, 2015, **625**, p 221–229

35. Y. Zhong, L. Liu, S. Wikman, D. Cui, and Z. Shen, Intragranular Cellular Segregation Network Structure Strengthening 316L Stainless Steel Prepared by Selective Laser Melting, *J. Nucl. Mater.*, 2016, **470**, p 170–178

36. D. Kong, C. Dong, X. Ni, L. Zhang, J. Yao, C. Man, X. Cheng, K. Xiao, and X. Li, Mechanical Properties and Corrosion Behavior of Selective Laser Melted 316L Stainless Steel after Different Heat Treatment Processes, *J. Mater. Sci. Technol.*, 2019, **35**(7), p 1499–1507

37. F.K. Yan, N.R. Tao, F. Archie, I. Gutierrez-Urrutia, D. Raabe, and K. Lu, Deformation Mechanisms in an Austenitic Single-Phase Duplex Microstructured Steel with Nanotwinned Grains, *Acta Mater.*, 2014, **81**, p 487–500

38. A.K. Agrawal and A. Singh, Limitations on the Hardness Increase in 316L Stainless Steel under Dynamic Plastic Deformation, *Mater. Sci. Eng., A*, 2017, **687**, p 306–312

39. T. Chen, L. Tan, Z. Lu, and H. Xu, The Effect of Grain Orientation on Nanoindentation Behavior of Model Austenitic Alloy Fe-20Cr-25Ni, *Acta Mater.*, 2017, **138**, p 83–91

40. G.T. Gray, V. Livescu, P.A. Rigg, C.P. Trujillo, C.M. Cady, S.R. Chen, J.S. Carpenter, T.J. Lienert, and S.J. Fensin, Structure/Property (Constitutive and Spallation Response) of Additively Manufactured 316L Stainless Steel, *Acta Mater.*, 2017, **138**, p 140–149

41. D.K. Patel and S.R. Kalidindi, Correlation of Spherical Nanoindentation Stress-Strain Curves to Simple Compression Stress-Strain Curves for Elastic-Plastic Isotropic Materials Using Finite Element Models, *Acta Mater.*, 2016, **112**, p 295–302

42. B. Al-mangour, R. Mongrain, and S. Yue, Coronary Stents Fracture: An Engineering Approach (Review), *Mater. Sci. Appl.*, 2013, **4**, p 606–621

43. P. Tang, H. Xie, S.E.N. Wang, X. Ding, Q.I. Zhang, H. Ma, J.I.E. Yang, S. Fan, M. Long, and D. Chen, Numerical Analysis of Molten Pool Behavior and Spatter Formation with Evaporation During Selective Laser Melting of 316L Stainless Steel, *Metall. Mater. Trans. B*, 2019, **50**(5), p 2273–2283

44. A. Aggarwal, S. Patel, and A. Kumar, Selective Laser Melting of 316L Stainless Steel: Physics of Melting Mode Transition and Its Influence on Microstructural and Mechanical Behavior, *JOM*, 2019, **71**(3), p 1105–1116

45. R. Biswal, A.K. Syed, and X. Zhang, Assessment of the Effect of Isolated Porosity Defects on the Fatigue Performance of Additive Manufactured Titanium Alloy, *Addit. Manuf.*, 2018, **23**, p 433–442

46. H. Gong, K. Rafi, H. Gu, G.D. Janaki-Ram, T. Starr, and B. Stucker, Influence of Defects on Mechanical Properties of Ti-6Al-4 V Components Produced by Selective Laser Melting and Electron Beam Melting, *Mater. Des.*, 2015, **86**, p 545–554

47. A. Mertens, S. Reginster, H. Paydas, Q. Contrepois, T. Dormal, O. Lemaire, and J. Lecomte-Beckers, Mechanical Properties of Alloy Ti-6Al-4 V and of Stainless Steel 316L Processed by Selective Laser Melting: Influence of out-of-Equilibrium Microstructures, *Powder Metall.*, 2014, **57**(3), p 184–189

48. H.D. Carlton, A. Haboub, G.F. Gallegos, D.Y. Parkinson, and A.A. MacDowell, Damage Evolution and Failure Mechanisms in Additively Manufactured Stainless Steel, *Mater. Sci. Eng., A*, 2016, **651**, p 406–414

49. L. Liu, Q. Ding, Y. Zhong, J. Zou, J. Wu, Y.L. Chiu, J. Li, Z. Zhang, Q. Yu, and Z. Shen, Dislocation Network in Additive Manufactured Steel Breaks Strength–ductility Trade-Off, *Mater. Today*, 2018, **21**(4), p 354–361

50. D. Karthik and S. Swaroop, Laser Shock Peening Enhanced Corrosion Properties in a Nickel Based Inconel 600 Superalloy, *J. Alloys Compd.*, 2017, **694**, p 1309–1319

51. K. Zaleski and A. Skoczylas, The Effect of the Conditions of Shot Peening the Inconel 718 Nickel Alloy on the Geometrical Structure of the Surface, *Adv. Sci. Technol.*, 2017, **11**(1), p 205–211

52. H.L. Chan, H.H. Ruan, A.Y. Chen, and J. Lu, Optimization of the Strain Rate to Achieve Exceptional Mechanical Properties of 304 Stainless Steel Using High Speed Ultrasonic Surface Mechanical Attrition Treatment, *Acta Mater.*, 2010, **58**, p 5086–5096

53. A.I. Dekhtyar, B.N. Mordyuk, D.G. Savvakin, V.I. Bondarchuk, I.V. Moiseeva, and N.I. Khripta, Enhanced Fatigue Behavior of Powder Metallurgy Ti–6Al–4 V Alloy by Applying Ultrasonic Impact Treatment, *Mater. Sci. Eng., A*, 2015, **641**, p 348–359

54. A. Boschetto, L. Bottini, and L. Sapienza, Surface Improvement of Fused Deposition Modeling Parts by Barrel Finishing, *Rapid Prototyp. J.*, 2015, **6**, p 686–696

55. H. Zhao, J. Van Humbeeck, J. Sohier, and I. De Scheerder, Electrochemical Polishing of 316L Stainless Steel Slotted Tube Coronary Stents, *J. Mater. Sci. Mater. Med.*, 2002, **13**(10), p 911–916

56. C.V. Vidal and A.I. Muñoz, Effect of Thermal Treatment and Applied Potential on the Electrochemical Behaviour of CoCrMo Biomedical Alloy, *Electrochim. Acta*, 2009, **54**(6), p 1798–1809

57. J. Cawley, J.E.P. Metcalf, A.H. Jones, T.J. Band, and D.S. Skupien, A Tribological Study of Cobalt Chromium Molybdenum Alloys Used in Metal-on-Metal Resurfacing Hip Arthroplasty, *Wear*, 2003, **255**(7–12), p 999–1006

58. B. Song, S. Dong, Q. Liu, H. Liao, and C. Coddet, Vacuum Heat Treatment of Iron Parts Produced by Selective Laser Melting: Microstructure, Residual Stress and Tensile Behavior, *Mater. Des.*, 2014, **54**, p 727–733

59. A. Schuessler, U. Bayer, G. Siekmeyer, R. Steegmueller, M. Strobel, and A. Schuessler, Optimize the Stent With New Manufacturing Technologies, *New Technol. Vasc. Biomater.*, 2007, **12**, p 93–106

60. H. Umeda, T. Gochi, M. Iwase, H. Izawa, T. Shimizu, R. Ishiki, H. Inagaki, J. Toyama, M. Yokota, and T. Murohara, Frequency, Predictors and Outcome of Stent Fracture after Sirolimus-Eluting Stent Implantation, *Int. J. Cardiol.*, 2009, **133**(3), p 321–326